



CrossMark  
 click for updates

Cite this: *RSC Adv.*, 2015, 5, 49861

## Synthesis and characterization of ZnO nanorods with a narrow size distribution†

Chandrakanth Reddy Chandraiahgari,<sup>\*ac</sup> Giovanni De Bellis,<sup>ac</sup> Paolo Ballirano,<sup>bc</sup> Santosh Kiran Balijepalli,<sup>d</sup> Saulius Kaciulis,<sup>d</sup> Luisa Caneve,<sup>e</sup> Francesca Sarto<sup>e</sup> and Maria Sabrina Sarto<sup>\*ac</sup>

The development of novel materials for energy harvesting applications or strain sensing has generated great interest towards zinc oxide (ZnO) nanostructures, and in particular towards the synthesis of ZnO nanowires or nanorods with well controlled morphology and properties. The high-yield mass production of such nanostructures by catalyst-free methods is a crucial aspect to enable a cost-effective large-scale development of new ZnO-based piezoelectric devices and materials. In the present work, we propose a method for the mass-production of high-purity ZnO-nanorods with a uniform size distribution, based on the combination of thermal decomposition of zinc acetate dihydrate and probe sonication in acetone. The quality of the produced ZnO nanorods is assessed through multi-technique characterization using field-emission scanning electron microscopy (FE-SEM), X-ray diffraction (XRD), transmission electron microscopy (TEM), X-ray photoelectron spectroscopy (XPS), and photo-luminescence spectroscopy (PL). The adopted synthesis method is simple, cost effective and feasible for large-scale production. Various process parameters such as precursor amount and growth time have been found to play an important role in controlling the formation of the as grown nanostructures with high uniformity in size and morphology. Size distribution curves were employed to depict the effect of various process parameters for tailoring the morphology, homogeneity and aspect ratio of the nanorods. Our results reveal that the high crystallographic quality of ZnO nanorods grown by a long-time thermal decomposition method is not affected by probe sonication, which is proposed as a post-synthesis step necessary to produce ZnO nanorod powder with a uniform distribution of diameters and lengths.

Received 10th February 2015  
 Accepted 21st May 2015

DOI: 10.1039/c5ra02631h

[www.rsc.org/advances](http://www.rsc.org/advances)

## Introduction

Zinc oxide (ZnO) is a significant technological material due to its remarkable performance in a wide range of multidisciplinary fields such as nanoscale optoelectronics, self-powered micro/nano systems, and nanomedicine.<sup>1–3</sup> It is a wide-band gap semiconducting material with a direct gap of 3.37 eV and a relatively large exciton binding energy of 60 meV at room temperature.<sup>4</sup> It crystallizes preferentially in the hexagonal wurtzite-type structure and forms a variety of nanostructures.<sup>5</sup> Such nanostructures exhibit unique optical, electronic, physical

and chemical properties owing to their size and morphology. Being a biosafe and biocompatible material and abundantly available for low cost fabrication techniques, it finds a wide range of existing or emerging commercial applications, including transparent UV shielding films, transparent conducting oxides, UV photo detectors, light-emitting diodes, solar cells, gas sensors, bio sensors, cosmetics, food product preservation, and nanoantibiotics.<sup>6–11</sup>

The rise in demand for large-scale amounts of engineered ZnO nanomaterials in diverse commercial products is due to their UV light absorption, semi-conducting, catalytic, and antibacterial properties. The enormous interest in ZnO is due to their unique ability of possessing structural dependent characteristics. It has been reported that the physical, chemical and optical properties of the nanostructures such as piezoelectricity, antimicrobial activity, photocatalytic activity and photo-luminescence are strongly dependent on ZnO structure size, shape and morphology.<sup>12–17</sup>

Many efforts have been devoted to the synthesis of aligned arrays of ZnO nanorods (NRs) or nanowires (NWs).<sup>10</sup> Vapor-liquid-solid synthesis (VLS) has been extensively explored in the literature as an approach to the formation of one-dimensional

<sup>a</sup>Department of Astronautics, Electrical and Energetics Engineering, Sapienza University of Rome, via Eudossiana 18, Rome 00184, Italy. E-mail: c.chandraiahgari@uniroma1.it; mariasabrina.sarto@uniroma1.it

<sup>b</sup>Department of Earth Sciences, Sapienza University of Rome, Piazzale Aldo Moro 5, Rome 00185, Italy

<sup>c</sup>Research Center on Nanotechnology Applied to Engineering of Sapienza (CNIS), SNNLab, Sapienza University of Rome, Piazzale Aldo Moro 5, Rome 00185, Italy

<sup>d</sup>CNR – ISMN, P.O. Box 10, 00015 Monterotondo Stazione, Rome, Italy

<sup>e</sup>ENEA, Centro Ricerche Frascati, Via Enrico Fermi 45, Frascati 00044, Italy

† Electronic supplementary information (ESI) available. See DOI: 10.1039/c5ra02631h

(1D) ZnO nanostructures such as whiskers, nanorods and nanowires.<sup>18–23</sup> The synthesis of ZnO nanorods *via* chemical approaches is an alternative to the aforementioned methods, opening a route to low-cost catalyst-free mass-production of ZnO nanostructures.<sup>24–28</sup>

In recent years, there has been an escalation in the development of various techniques for the large-scale synthesis of ZnO-NRs or NWs. Recently, the vapor phase thermal decomposition method (TDM)<sup>29,30</sup> and solution phase hydrothermal method (HTM)<sup>31,32</sup> have emerged as promising techniques for the synthesis of ZnO nanostructures, as they are simple, catalyst-free and inexpensive. These methods involve relatively few reaction steps, without the use or production of volatile and toxic substances, and they are suitable for large-scale production. However, the main difficulty of such techniques when applied for mass-production purposes is the selective control of the morphology of the grown nanostructures through the proper setting of the process parameters, in order to obtain the desired shape and dimensions, with minimum dispersion in diameter size and single-mode distribution of lengths. In a previous study,<sup>30</sup> it was reported that the aspect ratio and density of ZnO nanostructures synthesized by TDM can be controlled through the proper setting of growth temperature and duration. However, high-purity ZnO-NRs can be produced only with synthesis time is longer than several hours, as it was demonstrated by PL analysis.<sup>29</sup> The effect of precursor amount on the homogeneity and crystalline quality of the ZnO-NRs produced by TDM has not been extensively investigated yet. Similarly, it is known that precursor concentrations, growth temperature and duration have an influence on the morphology and aspect ratio of the nanostructures synthesized by HTM.<sup>32–34</sup> However, it is observed that in general TDM, compared to HTM, enables the synthesis of ZnO-NRs or NWs with a higher aspect ratio (defined as the ratio between length and diameter of a 1D structure) and better uniformity of diameter size and length along the axis. Therefore, it is of paramount importance for the development and understanding of the process parameters for the large-scale synthesis of ZnO nanostructures, enabling good control over morphology and a narrow size distribution.

In this work, we investigated the catalyst-free production route of ZnO nanorods with a uniform size distribution and high purity, through the combination of thermal decomposition of zinc acetate dihydrate and a post-synthesis step of probe sonication in acetone. The scope of this study is to develop a synthesis route of ZnO-NRs with uniform size distribution (in terms of diameter and length) and high purity, which is suitable for scaling up in mass-production applications, like piezoresistive or piezoelectric nanocomposites. Actually, the TDM, as presented in the literature,<sup>29</sup> leads to the production of ZnO-NRs with a wide distribution of lengths, ranging from a few hundred nanometers up to several microns.

In order to define the growth conditions suitable for the mass production of ZnO-NR powder, we investigated the effects of both precursor amount and growth period on the synthesis process. A multifunctional characterization of the produced nanomaterials was performed through field emission scanning electron microscopy (FE-SEM), X-ray diffraction (XRD),

transmission electron microscopy (TEM), X-ray photoelectron spectroscopy (XPS), and photo-luminescence spectroscopy (PL), in order to demonstrate the superior crystallographic properties of ZnO nanorods, treated or not by probe sonication, with respect to other types of ZnO structures such as microrods (MRs) and nanoparticles (NPs) synthesized by hydrothermal method as described in the ESI.† We show that probe sonication affects only the morphology of ZnO-NRs and can be used to obtain high-purity powders with narrow distribution of diameters ( $\sim 36 \text{ nm} \pm 10 \text{ nm}$ ) and single-mode distribution of lengths ( $\sim 470 \text{ nm} \pm 330 \text{ nm}$ ).

## Experimental

ZnO-NRs with uniform size distribution were produced starting from zinc acetate precursor through the five-step process sketched in Fig. 1 and described as follows.

### Materials

All chemicals were reagent grade and used as received without further purification: zinc acetate dihydrate ( $\text{Zn}(\text{CH}_3\text{COO})_2 \cdot 2\text{H}_2\text{O}$ , Sigma-Aldrich, ACS reagent,  $\geq 98\%$ ) and acetone ( $(\text{CH}_3)_2\text{CO}$ , Fisher Chemical, ACS reagent,  $\geq 99\%$ ).

### Synthesis of ZnO nanorods

ZnO-NRs were synthesized through the thermal decomposition method according to the procedure described by Chih-Cheng Lin *et al.*<sup>29</sup> In the typical synthesis process, a specific amount of zinc acetate dihydrate was distributed uniformly inside a disposable aluminum foil dish (TAAB, UK, 53 mm (diam.)  $\times$  17 mm (deep)) with an area of 22 cm<sup>2</sup>, closely packed with an aluminum foil, and finally placed inside a tightly closed steel box. The steel box was subsequently placed inside a preheated laboratory muffle furnace (Lenton UAF 15/10) at 300 °C in air for 12 h, producing porous papers of ZnO-NRs. Zinc acetate dihydrate served as the precursor for the synthesis and we did not use any other catalysts. The influence of precursor amount was evaluated using three different quantities, namely, 0.1 g, 0.3 g and 0.5 g, while maintaining the growth time for 12 h. The influence of short growth time of 3 h and 6 h was also evaluated for the precursor amount of 0.3 g.

ZnO-NR suspensions were produced by the dispersion of the ZnO-NR paper in acetone, with a concentration of 1 mg ml<sup>-1</sup>, by a probe sonication using a Sonics & Materials Vibracell VCX750. During the sonication, the suspensions were maintained at a constant temperature of 15 °C through a jacketed beaker, using a water bath circulator. After the sonication, ZnO-NRs powders was recollected with vacuum filtration with an alumina membrane (having a pore size of 20 nm) and was dried in oven at 120 °C for 15 min to remove any residual solvent. We performed two different sonication cycles:

(i) A short sonication (SS) in pulse mode (1 s on-phase and 1 s off-phase) for 5 min, with the ultrasound amplitude set at 40%, having the scope of uniformly dispersing ZnO-NRs, without altering their initial diameter and length, thus obtaining

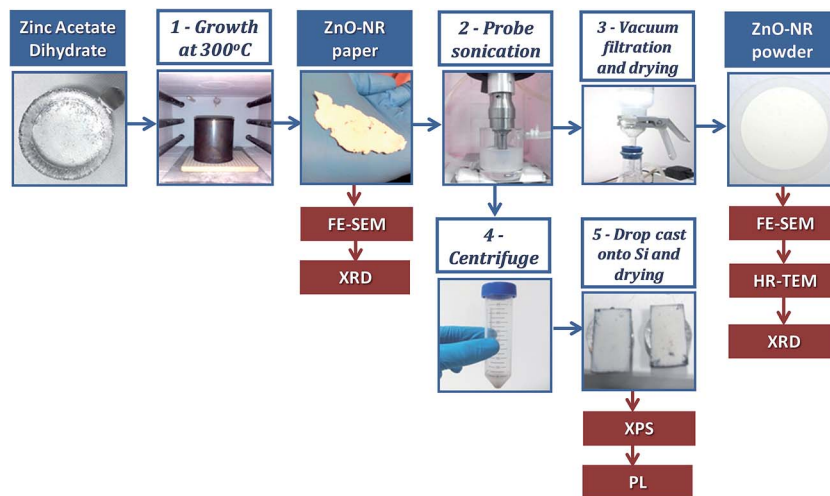


Fig. 1 Schematic of the ZnO-NRs production route and characterization process.

ZnO-NR powders with dual mode distribution of lengths, as shown in the section “Results”;

(ii) A long sonication (LS) in pulse mode (1 s on-phase and 1 s off-phase) for 20 min, with the ultrasound amplitude set at 70%, having the scope of chopping the longest nanowires in order to produce, after filtration, ZnO-NRs powder (NRL) characterized by a single-mode distribution of length.

### Characterizations

The morphology of the ZnO nanostructures was observed using a field emission scanning electron microscope (FE-SEM, Zeiss Auriga), which is available at SNN-Lab, at different steps of the production process, as sketched in Fig. 1. Samples for FE-SEM analysis were prepared by placing a small specimen of ZnO-NRs paper or a small amount of ZnO-NRs powder over an adhesive conductive copper tape. The papers were observed on both top and bottom faces and at fracture borders.

Numerically extrapolated probability distribution function (PDF) and empirical cumulative distribution function (CDF) curves were employed for the graphical representation of the size distribution of the ZnO-NRs (*i.e.* length and diameter), as per the FE-SEM observations. For this purpose, a minimum of 50 measurements of each physical dimension were recorded from the FE-SEM images.

The structural characterization and phase identification of the synthesized ZnO-NRs were performed by X-ray diffraction using a Bruker AXS D8-Advance diffractometer, operating in  $\theta$ - $\theta$  transmission geometry, equipped with focusing Göbel mirrors along the incident beam, Soller slits on both incident and (radial) diffracted beams, and a PSD VANTEC-1 detector. Samples were prepared by loading the powders into 0.3 mm diameter borosilicate capillaries that were aligned onto a standard goniometer head. XRD data were collected at room temperature (RT), using Cu K $\alpha$  radiation ( $\lambda = 1.5418 \text{ \AA}$ , 40 kV at 40 mA), in a  $2\theta$  angular range spanning from  $20^\circ$  to  $145^\circ$  with a step size of  $0.022^\circ$  and a counting time of 1 s. Structural

refinements were performed by the Rietveld method using TOPAS v.4.2 (Bruker AXS 2009) software.

Peak shape was modeled through the Fundamental Parameters Approach (FPA), imposing the following full axial parameters: divergence slit =  $0.3^\circ$ , source length = 12 mm, sample length and receiving slit length = 12.7 mm. The starting structural parameters of zincite were obtained from Sowa and Ahsbabs.<sup>35</sup> Absorption was modeled following the Sabine model for cylindrical samples<sup>36</sup> and the background was fitted by a Chebychev polynomial of the first kind. The occurrence of preferred orientation was tested by means of spherical harmonics (eight refinable parameters up to the 8th order). The selection of the number of terms to be used was performed following the procedure devised by Ballirano.<sup>37</sup> A marginal improvement of the fit was observed as a result of the near absence of texture, which is typical of a capillary mount. According to the shape of the crystallites, refinements were performed using the recently proposed ellipsoid-model of Katerinopoulou *et al.*<sup>38</sup> describing the diffraction-vector dependent broadening of diffraction maxima. In the hexagonal symmetry, the shape ellipsoid parameters  $b_{ij}$  are constrained as  $b_{11} = b_{22} = 2b_{12}$  and  $b_{13} = b_{23} = 0$ . The ellipsoid is oriented with the principal radii  $r_a \perp c$  and  $r_c \parallel c$ .

The crystallinity of the nanostructures was probed using transmission electron microscopy (TEM) using a FEI Tecnai F20 ST TEM operated at a beam energy of 200 keV. The samples for TEM were prepared by drop casting the ZnO-NR suspensions (produced either by SS or LS) onto lacey carbon coated 200 mesh Cu grids, with subsequent drying in air.

Samples for XPS and PL analyses were prepared from ZnO-NR suspensions (produced either by SS or LS). The concentrated solution of ZnO-NR suspension obtained upon centrifugation (at 193 g for 10 min) was drop-casted onto a cleaned silicon substrate, with subsequent drying in air.

Chemical composition and purity analysis was performed by X-ray photoelectron spectroscopy (XPS) and Auger electron spectroscopy (AES) using a monochromatized spectrometer

Escalab 250Xi (Thermo Fisher Scientific, UK) equipped with a six-channeltron detection system for spectroscopy. The measurements were performed using ZnO samples deposited on silicon substrates and placed inside an ultra-high vacuum (UHV) chamber, using the X-ray source set to the diameter of 900  $\mu\text{m}$ , the analyser at a constant pass energy of 20 eV and standard mode for the electromagnetic input lenses. Photoelectrons were excited using a standard Al K $\alpha$  excitation source, whereas spectroscopic data were processed by the Avantage v.5 software (Thermo Fisher Scientific, UK). The dependence of photoemission signal intensity on kinetic energy of photoelectrons from different core levels was included in the quantification procedure.

The optical properties and crystal defects of the ZnO nanostructures were studied with room temperature photoluminescence (PL) using the 266 nm line of a Nd:YAG pulsed laser (Thomson DIVA) as the excitation source, with a 10 ns pulse length and 20 Hz repetition rate. Crystalline silicon was chosen as the support for the ZnO nanostructures, because it was verified to not produce any PL signal under the considered laser excitation conditions. Energy dispersion of the PL signal was obtained using a 3648-element linear silicon CCD array, operating in the 200–1100 nm wavelength range. The PL spectra were repeated on each sample at three different levels of the laser mean power (*i.e.* 700, 900 and  $1300 \pm 100 \text{ W m}^{-2}$ ), to investigate the possible different behavior of defect-related and intrinsic PL signals. Each spectrum was repeated 16 times on the same sample and subtracted from the background acquired by blocking the laser source. The average values are reported *versus* the emission energy, as shown in Fig. 9. The standard deviation of the PL peak values ranged from 4% to 15%, depending on the PL intensity; the data in the interval of 525–540 nm were omitted to filter out the strong reflection signal at 532 nm by the 2nd harmonic of the incident laser source.

FE-SEM imaging and XRD were also performed on the ZnO-NRs produced either by SS or LS, after vacuum filtration of the suspensions and drying of the so-obtained residual material in an oven at 120 °C for 15 min, to remove any residual solvent.

## Results

ZnO-NRs were synthesized through a TDM. FE-SEM analysis reveals that the as-grown NRs are arranged in the form of a porous paper as shown in the ESI (Fig. S2†), characterized by a different morphology of the ZnO-NRs grown either on the top or bottom side or across the section.

The synthesis of the nanostructures was carried out using the precursor zinc acetate dihydrate at three different amounts (by weight), namely, 0.1 g, 0.3 g, and 0.5 g, while maintaining the fixed growth time of 12 h in a muffle furnace at 300 °C, and with an amount of precursor of 0.3 g considering increasing growth times of 3 h, 6 h and 12 h at a constant temperature of 300 °C. The produced ZnO-papers are reported in Table 1. The production yield was obtained in the range between 30% and 34%, which is close to its theoretical yield of 37%.<sup>29</sup> The total

Table 1 ZnO-NR papers produced under different experimental conditions (precursor amount and growth time): measured weight and production yield

ZnO-paper	Zinc acetate dihydrate (g)	Growth time (h)	Weight (mg)	Yield rate (wt%)
P1	0.1	12	34.2	34.2
P2	0.3	12	90.3	30.1
P3	0.5	12	157.3	31.4
P4 <sup>a</sup>	0.3	3	96.9	32.3
P5	0.3	6	91.7	30.6

<sup>a</sup> Due to the short synthesis time the P4 assumes the form of a sponge-like porous material, as shown in the ESI.

amount of produced ZnO-NRs increased proportionally to the precursor amount.

The fracture section of ZnO-NR papers produced with different precursor amounts of 0.1 g and 0.3 g are observed by FE-SEM and are shown in the ESI (Fig. S1A and S1B,† respectively). It can be noted that NRs having lengths longer than a few microns can be observed only on the top side of the paper obtained using 0.3 g of precursor (Fig. S1B†).

It is observed that the morphology (*i.e.* diameter and length) of the ZnO-NRs grown on the bottom side of the paper are quite different from the nanostructures grown on the top side, as shown in Fig. 2A–F. In particular, for increasing the amount of precursor (*i.e.* from 0.1 g to 0.5 g), the difference in length and diameter of the ZnO-NRs observed on the top and bottom sides of the paper also increased. Papers produced with 0.1 g of precursor consist of ZnO-NRs with a diameter below 100 nm on both sides. Nevertheless, on the top face there are NRs with lengths up to a micron (Fig. 2A), whereas the ZnO nanostructures observed on the bottom have a length limited to a few hundreds of nanometers (Fig. 2B). In the case of 0.3 g of precursor, the papers are made of longer ZnO-NRs on the top face (Fig. 2C) than on the bottom one (Fig. 2D), where the average lengths of the ZnO nanostructures is limited to a few hundreds of nanometers, and we also observed the formation of some clusters of very short NRs. Finally, the papers produced with 0.5 g of precursor are characterized on the top side by a uniform distribution of NRs, with a diameter in the range of 20–40 nm (Fig. 2F). On the contrary, the bottom side of such papers consists of ZnO rods with a diameter ranging from 20–30 nm (*i.e.* NRs) up to a few hundreds of nanometers (*e.g.* MRs) (Fig. 2G).

We also investigated the effect of the growth time on the morphology of the ZnO-NRs on the top face of the paper produced with 0.3 g of precursor. We noticed that after only 3 h, the produced porous material has the form of a sponge, composed of ZnO-NRs with an average length of  $\sim 390$  nm. In that case, we did not observe an organized stratification of the porous material, with relevant morphological differences between ZnO-NRs grown in different positions. After 6 h of growth time, we observed the formation of a paper-like porous paper, with a stratification of ZnO-NRs assuming different morphology on the top and bottom faces; in particular, the NRs

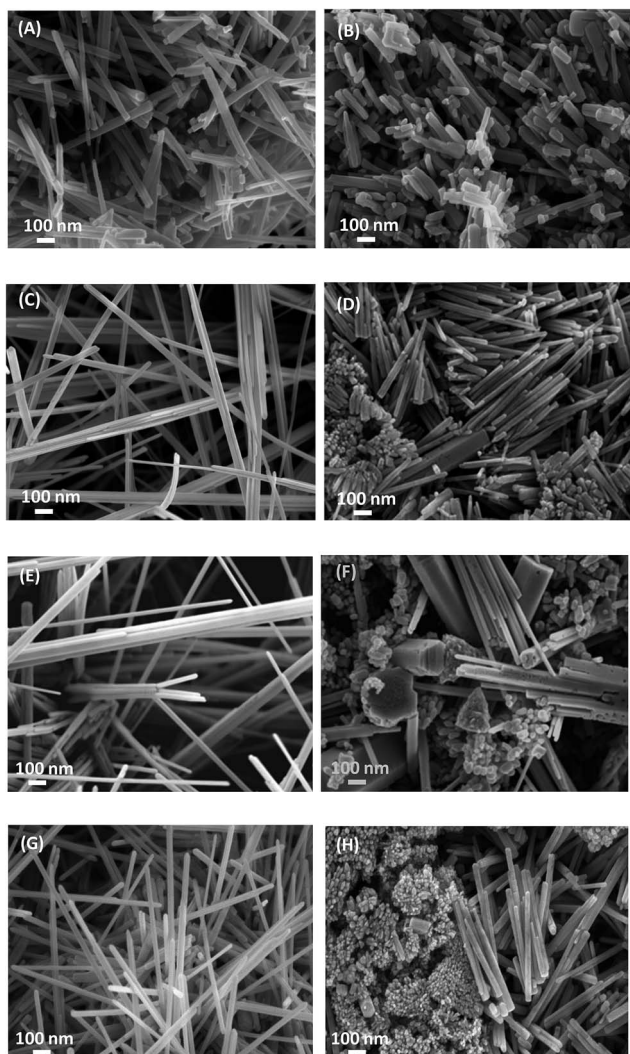


Fig. 2 FE-SEM images of ZnO-NRs on the top (A, C, E and G) and bottom (B, D, F and H) faces of the porous paper grown under different conditions: 0.1 g of precursor and 12 h at 300 °C (A and B); 0.3 g of precursor and 12 h at 300 °C (C and D); 0.5 g of precursor and 12 h at 300 °C (E and F); 0.3 g of precursor and 6 h (G and H) at 300 °C.

grown on the top side of the porous paper (Fig. 2G) have a very similar morphology with respect to the ones grown after 12 h (Fig. 2C).

Table 2 summarizes the estimated mean values and standard deviations of diameter and length of ZnO-NRs observed on the top and bottom faces of the produced papers, as they result from FE-SEM analyses. It can be observed that the ZnO-NR diameter gets larger as the precursor amount increases, setting the growth time at 12 h. The higher values of standard deviation are representative of a larger presence of aggregates. In this study, the synthesis of ZnO-NRs using 0.3 g of precursor amount is considered as an optimum choice in the range 0.1–0.5 g, because it represents the best compromise to have an NR average diameter below 50 nm and length up to a few microns.

Table 2 Mean values and standard deviations (in brackets) of diameter and length of ZnO-NRs on the top or bottom sides (indicated as NRxT and NRxB respectively) of the papers listed in Table 1 and obtained by LS of the paper P2 (indicated as NRxL)

ZnO-NR	ZnO-paper	Sonication	Diameter (nm)	Length ( $\mu\text{m}$ )
NR1T	P1	No	36 (11)	0.43 (0.17)
NR1B	P1	No	45 (18)	0.17 (0.10)
NR2T	P2	No	36 (10)	2.67 (0.58)
NR2B	P2	No	46 (24)	0.17 (0.10)
NR3T	P3	No	39 (15)	2.67 (1.11)
NR3B	P3	No	65 (39)	1.39 (0.40)
NR4T	P4	No	35 (10)	0.39 (0.23)
NR5T	P5	No	35 (11)	0.79 (0.38)
NR5B	P5	No	33 (12)	0.20 (0.13)
NR2L	P2	LS	36 (10)	0.47 (0.33)

The growth of ZnO NRs is understood further by the experiments carried out with a shorter reaction growth time, *i.e.* only for 3 and 6 h with a precursor amount of 0.3 g. For the growth time of 3 h, we noticed that the average length of the grown NRs is limited to  $\sim 390$  nm, whereas after 6 h it reaches  $\sim 790$  nm. Moreover, a previous study has demonstrated that ZnO-NRs grown by TDM improve their photoluminescence properties with increasing growth time.<sup>29</sup> Therefore, in the following discussion we focused our study only on ZnO-NRs produced from the paper P2.

ZnO-NRs are obtained by the probe sonication of the produced papers in acetone. We observed through FE-SEM imaging that a SS does not affect the remarkable length and diameter of the ZnO-NRs (Fig. 3A and B). On the contrary, a more homogeneous size distribution of ZnO-NRs was obtained after LS of the P2 paper, as reported in Table 2. We noticed that ZnO-NRs were chopped during LS, but their diameter was not affected, as shown in Fig. 3C and D. A similar effect was noticed also on ZnO-MRs, as reported in the ESI.†

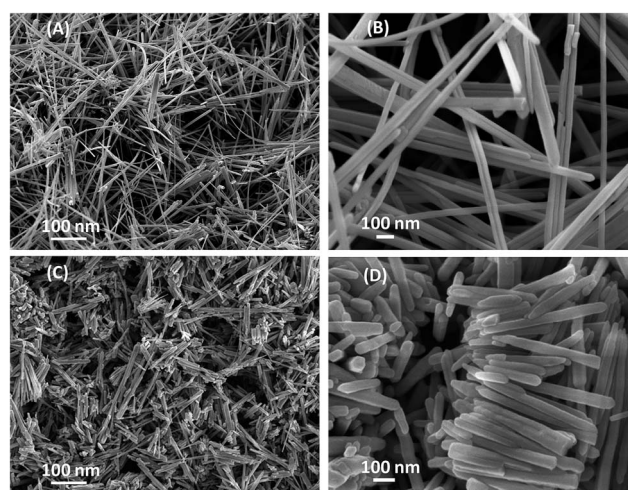


Fig. 3 FE-SEM images of ZnO-NRs produced through SS (A and B) or LS (C and D) in acetone of the porous paper grown for 12 h at 300 °C using 0.3 g of precursor.

The cumulative distribution function (CDF) of lengths for the different types of ZnO-NRs produced using 0.3 g of precursor (Table 2) was calculated and reported in Fig. 4A. We noticed that for increasing growth time, the dispersion between the CDFs at 50% associated to NRs on the top and bottom sides of the same paper rises up (from  $\sim 0.6 \mu\text{m}$  for 6 h growth time to  $\sim 2.5 \mu\text{m}$  for 12 h growth time). The 50% CDF for ZnO-NRs produced by LS of the paper P2 corresponds to the length of  $0.47 \mu\text{m}$ . The diameter CDF of the ZnO-NRs produced by LS of the paper P2 is reported in Fig. 4B; it is confirmed that the LS does not affect remarkably the nanorods diameter.

Therefore, we assumed that LS can be used for the production of ZnO-NRs with a single-mode length distribution. In order to validate this assumption, we investigated the structural and optical properties of the produced nanostructures, described as follows.

The crystalline structure of the ZnO-NRs powders, produced by SS and LS of the paper P2 in acetone, was evaluated by XRD analysis. Fig. 5 shows the recorded diffraction patterns of the synthesized ZnO-NRs produced by LS (NR2L) or by SS (NR2S), compared with the ones of ZnO-MRs (MR) and of ZnO-NPs (NP) synthesized, as described in the ESI.† The sharp and intense

peaks of the spectra, shown in Fig. 5, demonstrate the highly crystalline nature of the synthesized ZnO structures. Moreover, all four diffraction patterns are in good agreement with the one published in the Joint Committee on Powder Diffraction Standards (JCPDS) card 036-1451 for the hexagonal wurtzite structure of ZnO.

A careful scrutiny of the diffraction patterns, shown in Fig. 5, confirms the absence of any detectable crystalline impurity, within the limits of the diffractometer sensitivity, which is estimated to be of *ca.* 0.1 wt%.

The structural information of the analyzed micro- and nano-structures is reported in Table 3. Zincite has the hexagonal ZnS wurtzite structure, and it is characterized by cell parameters and the volume of the reference sample that are smaller than those of all micro- and nano-structures investigated in this study, which is in agreement with previous findings on other simple oxides.<sup>39–41</sup> All analyzed samples show a  $\langle \text{Zn-O} \rangle$  bond distance of  $1.978 \text{ \AA}$  in perfect agreement with the findings of Sowa and Ahsbahs.<sup>35</sup> Moreover, the  $\Delta$  polyhedral distortion ( $\times 10^4$ ) (as defined by Brown and Shannon)<sup>42</sup> is always lower or equal to 0.09, thus confirming the substantial regularity of the  $\text{ZnO}_4$  tetrahedron.

However, NR2L, NR2S, NP and reference sample SA06 show the  $\text{Zn-O} \times 3$  bond distances that are lying in the *xy* plane and are shorter ( $\langle \text{Zn-O} \times 3 \rangle = 1.9753(8) \text{ \AA}$ ) than the remaining one ( $\langle \text{Zn-O} \rangle = 1.986(3) \text{ \AA}$ ), which is aligned along the *z* direction. Instead, MR is characterized by an almost perfectly regular tetrahedron. In addition, MR has a displacement parameter of the O site smaller than that of the Zn site, whereas all the remaining samples show comparable values for both sites. Finally, MR is characterized by cell parameters that are significantly larger than those of the other samples.

Following the finding of Kaurova *et al.*,<sup>43</sup> we investigated the possible symmetry reduction from  $P6_3/mc$ , which is typical of stoichiometric zincite, to  $P3$ , which has been observed in O-defective zincite. However, no Bragg reflection at *ca.*  $17.2^\circ 2\theta$ , which is attributed by the authors to the symmetry-violating 001 peak, was observed in all the analyzed samples indicating that the correct space group for the present nano-structured zincites

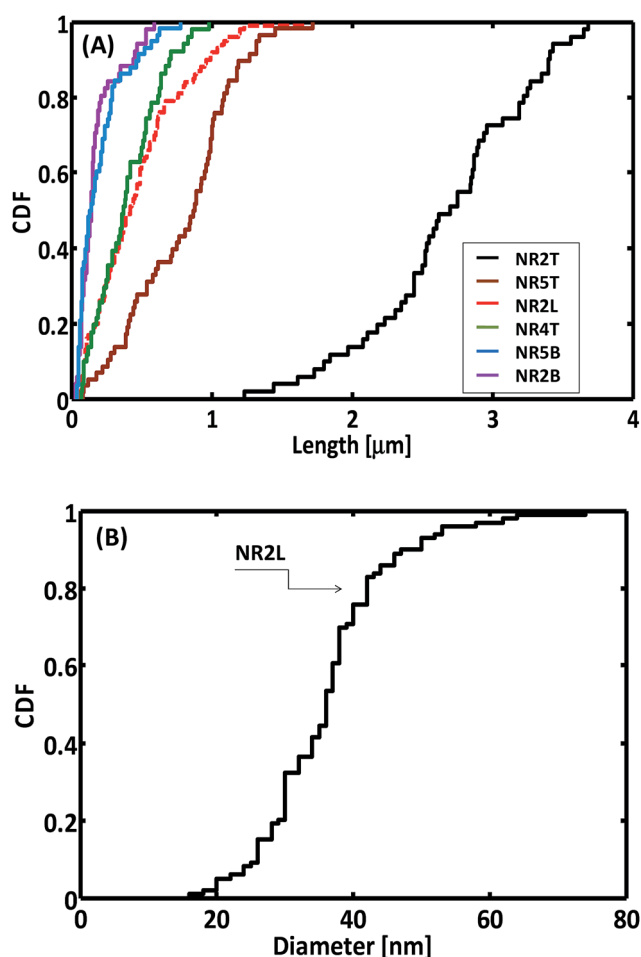


Fig. 4 Length CDF of ZnO-NRs produced with 0.3 g of precursor (A) and diameter CDF of the NRs obtained by LS of the paper P2 (B).

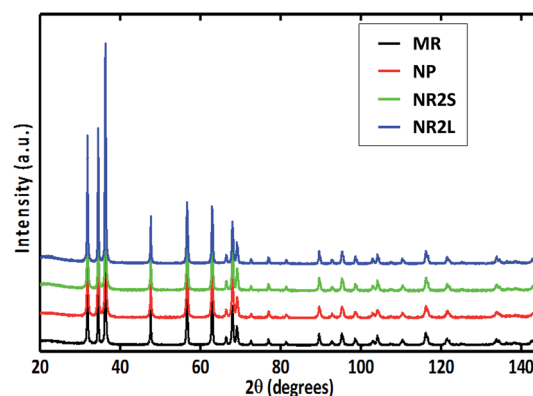


Fig. 5 X-ray diffraction patterns of ZnO-NRs produced from paper P2 by SS and LS, and of ZnO-MRs and ZnO-NPs synthesized as described in the ESI.†

**Table 3** Cell parameters  $a$ ,  $c$ ,  $a/c$ , volume, bond distances and tetrahedral distortion ( $\Delta \times 10^4$ ) of the analysed ZnO samples. Reference data SA06 (ref. 33) from single-crystal analysis are reported for comparison purposes

	MR	NR2L	NR2S	NP	SA06
$a$ (Å)	3.25110(2)	3.24979(2)	3.24989(2)	3.24987(2)	3.2494(2)
$c$ (Å)	5.20831(4)	5.20637(4)	5.20653(4)	5.20694(5)	5.2054(2)
$c/a$	1.6020	1.6021	1.6021	1.6022	1.6020
Volume (Å <sup>3</sup> )	47.6748(7)	47.6186(7)	47.6231(6)	47.6261(8)	47.598(7)
Zn $B_{\text{iso}}$ (Å <sup>2</sup> )	0.506(9)	0.488(8)	0.493(8)	0.493(8)	*0.52(3)
O $B_{\text{iso}}$ (Å <sup>2</sup> )	0.35(4)	0.47(4)	0.50(4)	0.40(3)	*0.58(15)
Zn–O $\times 3$ (Å)	1.9792(7)	1.9762(6)	1.9752(6)	1.9745(6)	1.974
Zn–O (Å)	1.977(2)	1.983(2)	1.986(2)	1.988(2)	1.988
$\langle \text{Zn–O} \rangle$	1.978	1.978	1.978	1.978	1.978
$\Delta$	0.01	0.02	0.06	0.09	0.09

is  $P6_3/mc$ . According to Kaurova *et al.*,<sup>43</sup> the occurrence of O-vacancies is coupled to a marked reduction of the cell parameters, which is not observed in the present samples. The analysis of the micro structural parameters indicates that  $\epsilon_0$  micro-strain (lattice strain), which is defined as  $\beta_i = 4\epsilon_0 \tan \theta$  ( $\beta_i$  being the peak integral breadth),<sup>44</sup> takes the larger value of 0.0660(7) in the case of NP. The same sample has a nearly spherical coherency domain ellipsoid of *ca.* 60 nm in diameter, which is in excellent agreement with the average grain size of 66(20) nm determined from FE-SEM. The remaining samples are characterized by a marked asymmetry of the principal radii of the coherency domain ellipsoid that shows  $r_c/r_a$  ratios ranging from 1.75(2) and 2.05(3).

The coherency domains along the  $a$ -axis calculated for ZnO-NRs produced by SS and LS and for ZnO-MRs are consistent with their diameters as observed by FE-SEM, whereas the ones estimated along the  $c$ -axis are significantly shorter than the ZnO-NRs and MRs lengths. Such an apparent discrepancy may be justified by polycrystallinity, as it seems to be confirmed by the observation that the principal radii of ZnO-NRs (obtained by LS and SS) are virtually unchanged, indicating that sonication has probably acted as a disaggregation medium.

TEM analysis was performed on the samples produced by SS and LS of the paper P2 in acetone. Fig. 6A and B show high resolution TEM (HR-TEM) images of the synthesized ZnO-NRs produced by SS (NR2S) and by LS (NR2L), respectively. The micrographs demonstrate that the nanorods are perfectly crystalline and oriented along the [100] direction, as clearly indicated by the FFT (in the inset). The structure of the NR2L sample, even if perfectly crystalline, appears slightly more damaged, in particular over the surface. Furthermore, images of Z-contrast high angle annular dark field (HAADF) scanning transmission electron microscopy (STEM) of the ZnO-NR produced by SS and LS are reported in the ESI (Fig. S4 and S5<sup>†</sup>), together with the results of energy dispersive X-ray (EDX) spectroscopy. The HAADF-STEM and EDX analyses revealed that Zn and O are the only elements present in the crystalline structure. The observed composition is uniform with stoichiometry close to ZnO.

The surface chemical compositions of the ZnO-NRs obtained by LS and SS have been analyzed by XPS in order to detect any

trace of impurities and to assess the homogeneity of sample composition. The obtained data are compared with the data obtained for ZnO-MRs and ZnO-NPs (synthesized according to the procedure described in the ESI<sup>†</sup>). In all the samples, zinc is present in the form of ZnO, *i.e.* in the Zn(+2) chemical state, which is evident from the binding energy (BE) value of Zn 2p<sub>3/2</sub> peak at BE  $\approx$  1021.3 eV and from the Auger Zn LMM peak position at a kinetic energy (KE) of  $\approx$  988.3 eV.<sup>45,46</sup> In addition, the value of the modified Auger parameter  $\alpha \approx$  2010.5 eV corresponds to the Zn(+2) chemical state.<sup>45,47</sup> The spectra of Zn 2p and Zn LMM regions are shown in Fig. 7A and B, respectively. The O 1s spectra of all the ZnO-NRs samples consists of two components indicated as O 1s A and O 1s B. The first component is attributed to O<sub>2</sub><sup>−</sup> ions in the wurtzite structure of ZnO,<sup>44</sup> whereas the second one is attributed to the loosely bound oxygen on the surface, such as in adsorbed hydroxyl groups –OH and/or –CO<sub>3</sub> radicals.<sup>45,48</sup> The O 1s spectra of the ZnO-NRs samples including the peak fitting are presented in Fig. 8A and B. The C 1s spectra are similar for both samples and indicate the presence of the aliphatic carbon (component C 1s A) and carbonates (C 1s B). For better understanding of the differences between the samples, the ratio of Zn and O was computed for the component of oxide O 1s A. In the case of Zn/O > 1, the amount of O is lower in comparison with stoichiometric oxide. In this situation, the lack of oxygen is an indicator of the higher number of defects in zinc oxide. The

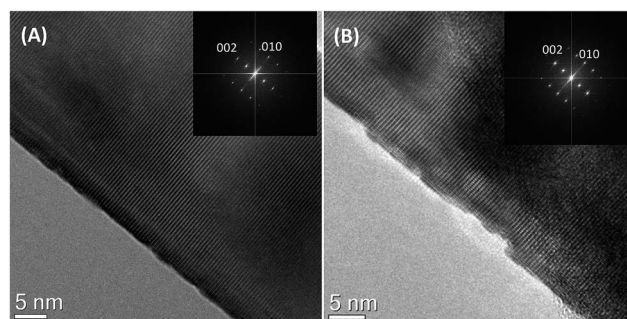


**Fig. 6** HR-TEM images of the ZnO NR produced from paper P2 by (A) SS and (B) LS samples. The crystal is oriented along the [100] direction as clearly indicated by the FFT (in the inset).

Zn/O ratios were computed for ZnO-NRs, ZnO-MRs, and ZnO-NPs. The obtained results demonstrated that MRs have the highest number of defects and the NRs obtained by SS have a considerably lower number. The occurrence of a more extended defectivity agrees with the reported significantly larger cell parameters of MR as compared to the remaining samples. For the different types of ZnO micro/nanostructures the results are as follows: for MR Zn/O a ratio equal to 1.35; for NR2L, it is 1.3; for NPs, it is 1.2; for NR2S, the Zn/O ratio is 1. These results indicate that our preparation method ensured the production of pure oxide in all four nanostructures of ZnO products, as the Zn and O were the only elements detected on the surface. Furthermore, the obtained spectra revealed that LS induces the presence of surface oxygen defects in ZnO-NRs.

Photoluminescence spectra of the ZnO-NRs produced with SS and LS have been registered at room temperature and compared to those of MRs and NPs in order to investigate the presence of defects. As it is well known, defects in semiconductor materials will induce energy levels in their band gaps, causing the quenching of direct band edge (BE) emission and eventually activating PL bands at lower emission energy.

In ZnO nanostructures, BE emission is typically observed as a sharp ultraviolet (UV) peak at  $\sim 3.3$  eV (380 nm).<sup>49,50</sup> In

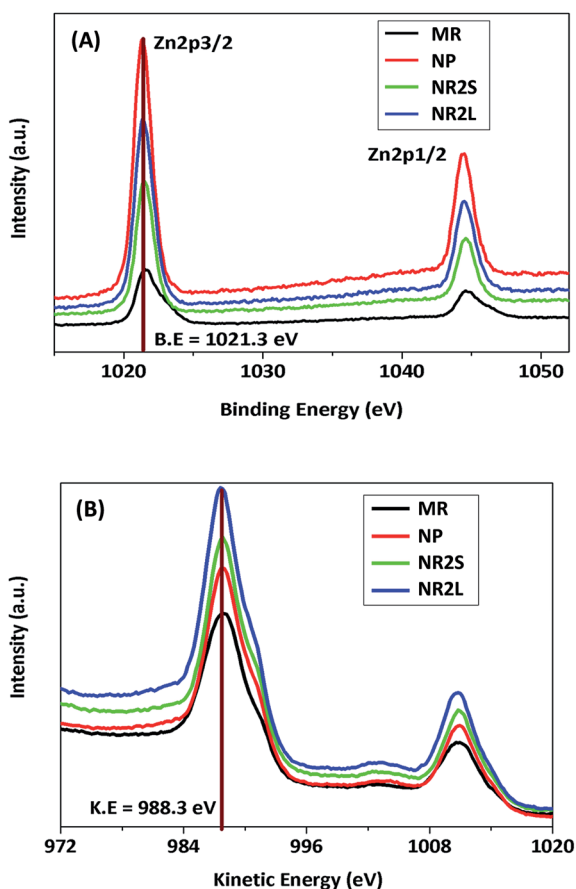


Fig. 7 Zn 2p spectra (A) and Auger Zn LMM spectra (B) of ZnO-NRs produced from paper P2 by SS and LS and of ZnO-MRs and ZnO-NPs synthesized as described in the ESI.†

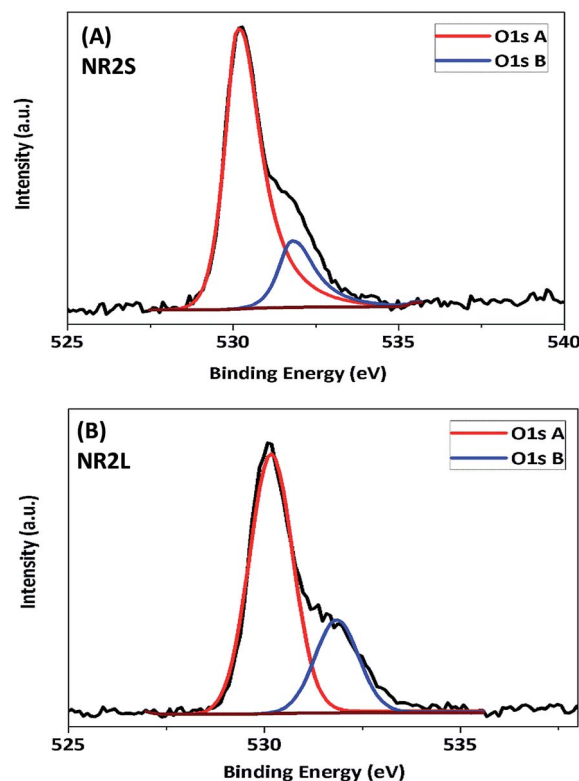


Fig. 8 O 1s spectra of ZnO-NRs produced from paper P2 by SS (A) and LS (B).

addition, different types of defects such as oxygen vacancies, interstitial oxygen, zinc vacancies and interstitial zinc have been reported to contribute to various visible (VIS) bands in the 470–630 nm range of PL spectra of ZnO nanocrystals.<sup>51–54</sup> In particular, for ZnO nano-rods it has been also proposed that the visible band around  $\sim 2.1$  eV originates from defects localized near the outmost surface of the nanostructures, within a region of few tens of nanometers.<sup>55</sup> It is also quite intuitive and accepted that structural defects may segregate at surface and grain boundary sites due to the small dimension of the nanocrystals.

In general, the ratio between UV and VIS PL peak intensity is taken as an indicator of defect concentration of ZnO nanostructures.<sup>54,56,57</sup> This is true as long as the pumping rate does not exceed the surface-recombination rate, *i.e.*, a high enough pumping rate may still produce band-to-band recombination because the surface states are only capable of recombining a limited number of carriers at a given time. For this reason, PL measurements on our samples have been repeated by varying the laser fluence, as reported in ESI.†

The PL spectra of both ZnO-NRs produced with SS or LS are reported in Fig. 9, and they show only a quite intense UV exciton peak at  $\sim 3.26$  eV and no other emission in all the visible range. The results are obtained for  $1300 \text{ W m}^{-2}$  and are in line with those at lower power levels (described in ESI†). Differently, for the ZnO-MRs, the PL spectrum is dominated by a strong broad visible band with maximum emission at  $\sim 2.13$  eV, while the very weak band gap emission at  $\sim 3.26$  eV is hardly detectable at



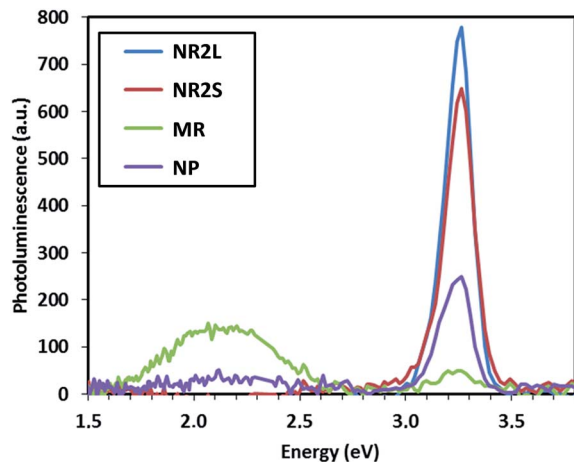


Fig. 9 Photoluminescence spectra of ZnO-NRs produced from paper P2 by SS and LS, and of ZnO-MRs and ZnO-NPs synthesized as described in the ESI; † incident laser power =  $1300 \text{ W m}^{-2}$ .

the higher laser power levels and it is completely quenched at  $700 \text{ W m}^{-2}$ .

Peak intensities of UV and VIS emissions are summarized in Table 4 for all samples and laser power levels. The results indicate that defect concentration is lower in both LS and SS NRs, because their UV peak intensity is higher and their VIS/UV ratios are lower than the corresponding NPs and MRs. Furthermore, it is noted that UV peak intensity is similar, within the experimental error, for NRs produced by LS and SS. This result is consistent with XRD analysis, showing that the principal radii of ZnO-NRs are virtually unchanged by LS or SS treatment and suggesting that sonication probably acted as a disaggregation medium of the polycrystalline NRs. This consideration is not in contradiction to the TEM and XPS results, indicating that LS induces the presence of surface oxygen defects in ZnO-NRs. In fact, XPS and PL analysis may reveal different types of defects; XPS is sensitive to the oxygen vacancies located at the outmost surface of the nanostructures,

Table 4 Peak intensities of the UV and Vis emissions of the produced material samples (i.e. MR, NP, NR2L and NR2S) with increasing laser power intensity

Sample	Power ( $\text{W m}^{-2}$ )	UV PL intensity (a.u.)	VIS PL intensity (a.u.)
MR	$700 \pm 100$	$0 \pm 10$	$90 \pm 10$
	$900 \pm 100$	$28 \pm 9$	$100 \pm 10$
	$1300 \pm 100$	$50 \pm 8$	$140 \pm 10$
NP	$700 \pm 100$	$50 \pm 8$	—
	$900 \pm 100$	$110 \pm 10$	—
	$1300 \pm 100$	$250 \pm 10$	$20 \pm 10$
NR2L	$700 \pm 100$	$110 \pm 10$	—
	$900 \pm 100$	$350 \pm 20$	—
	$1300 \pm 100$	$780 \pm 60$	—
NR2S	$700 \pm 100$	$80 \pm 10$	—
	$900 \pm 100$	$250 \pm 10$	—
	$1300 \pm 100$	$650 \pm 30$	—

whereas PL may be also affected by defects occurring at grain boundaries, even if they are embedded inside the nanostructure.

## Conclusions

In the present work, we proposed a synthesis route based on the thermal decomposition method, for the mass production of high-purity ZnO-NRs with controlled morphology, uniform diameter, and single-mode length distribution. The proposed approach combines thermal decomposition of zinc acetate dihydrate with probe sonication in acetone.

A multi-technique characterization of the produced nanostructures is approached in order to validate the proposed synthesis route, through the assessment of ZnO structural and physical properties.

The optimum precursor amount of 0.3 g for the growth time of 12 h at  $300 \text{ }^\circ\text{C}$  allows the production of ZnO-NRs with high purity, but dual-mode distribution of the nanostructure lengths. We demonstrated that probe sonication in pulsed mode of the synthesized ZnO-NR porous materials dispersed in acetone, for 20 min with an ultrasound amplitude of 70%, does not affect the diameter, purity and photoluminescence properties of the 1D nanostructures, but it enables us to obtain ZnO-NR powders with single-mode distribution of lengths, with an average value of  $\sim 470 \text{ nm}$ .

The PL spectra of the produced ZnO-NRs indicates the excellent quality of the nanostructures, because their UV emission is considerably higher than that detected in ZnO-MRs and ZnO-NPs samples and no visible emission is observable in the entire investigated energy range (down to 1.4 eV) and laser power levels ( $700\text{--}1300 \text{ W m}^{-2}$ ).

We can conclude that the proposed production route of ZnO-NRs characterized by uniform size distribution is suitable for large-scale applications. The possibility to control the ZnO-NR morphology, which is combined with a cost-effective synthesis route, enabling mass production and guaranteeing high quality, makes these nanostructures suitable for use as filler in a polymeric matrix for the development of new piezoresistive and piezoelectric materials.

## Acknowledgements

We are thankful to Dr Vittorio Morandi and Dr Andrea Migliori (CNR-IMM Section of Bologna, Italy) for performing TEM analyses, HR-TEM imaging, HAADF-STEM and EDX spectroscopy, and for their helpful comments and discussion.

## References

- 1 S. Xu and Z. L. Wang, *Nano Res.*, 2011, **4**, 1013.
- 2 Z. L. Wang and W. Wu, *Angew. Chem., Int. Ed.*, 2012, **51**, 11700.
- 3 Ae J. Huh and Y. J. Kwon, *J. Controlled Release*, 2011, **156**, 128.
- 4 C. Klingshirm, *ChemPhysChem*, 2007, **8**, 782.
- 5 Y. Zhang, M. K. Ram, E. K. Stefanakos and D. Y. Goswami, *J. Nanomaterials*, 2012, **2012**, 624520.

- 6 D. Sun, N. Miyatake and H.-J. Sue, *Nanotechnology*, 2007, **18**, 215606.
- 7 U. Ozgur, D. Hofstetter and H. Morkoc, *Proc. IEEE*, 2010, **98**, 1255.
- 8 Q. Zhang, S. D. Christopher, X. Zhou and G. Cao, *Adv. Mater.*, 2009, **21**, 4087.
- 9 P. J. Perez Espitia, N. de Fátima Ferreira Soares, J. Sélia dos Reis Coimbra, N. J. de Andrade, R. Souza Cruz, E. Antonio and A. Medeiros, *Food Bioprocess Technol.*, 2012, **5**, 1447–1464.
- 10 D. Bekermann, *et al.*, *ChemPhysChem*, 2010, **11**, 2337–2340.
- 11 D. Barreca, *et al.*, *Sens. Actuators, B*, 2010, **149**, 1–7.
- 12 G.-C. Yi, C. Wang and W. I. Park, *Semicond. Sci. Technol.*, 2005, **20**, S22.
- 13 C. Falconi, G. Mantini, A. D'Amico and Z. L. Wang, *Sens. Actuators, B*, 2009, **139**, 511.
- 14 I. Rago, C. Reddy Chandraiahgari, M. P. Bracciale, G. De Bellis, E. Zanni, M. Cestelli Guidi, D. Sali, A. Broggi, C. Palleschi, M. S. Sarto and D. Uccelletti, *RSC Adv.*, 2014, **4**, 56031.
- 15 C. C. Chen, N. Ye, C. F. Yu and T. Fan, *J. Ceram. Process. Res.*, 2014, **15**, 102.
- 16 S. S. Warule, N. S. Chaudhari, B. B. Kale and M. A. More, *CrystEngComm*, 2009, **11**, 2776.
- 17 P. Rai, S. Raj, In-H. Lee, W.-K. Kwak and Y.-T. Yun, *Ceram. Int.*, 2013, **39**, 8287.
- 18 M. H. Huang, Y. Wu, H. Feick, N. Tran, E. Weber and P. Yang, *Adv. Mater.*, 2001, **13**, 113.
- 19 Y. W. Wang, L. D. Zhang, G. Z. Wang, X. S. Peng, Z. Q. Chu and C. H. Liang, *J. Cryst. Growth*, 2002, **234**, 171.
- 20 P. Yang, H. Yan, S. Mao, R. Russo, J. Johnson, R. Saykally, N. Morris, J. Pham, R. He and H.-J. Choi, *Adv. Funct. Mater.*, 2002, **12**, 323.
- 21 S. Y. Li, C. Y. Lee and T. Y. Tseng, *J. Cryst. Growth*, 2003, **247**, 357.
- 22 W. I. Park, D. H. Kim, S. W. Jung and G. C. Yi, *Appl. Phys. Lett.*, 2002, **80**, 4232.
- 23 W. I. Park, G. C. Yi, M. Y. Kim and S. J. Pennycook, *Adv. Mater.*, 2002, **14**, 1841.
- 24 B. Liu and H. C. Zeng, *J. Am. Chem. Soc.*, 2003, **125**, 4430.
- 25 Z. Q. Li, Y. Xie, Y. J. Xiong, R. Zhang and W. He, *Chem. Lett.*, 2003, **32**, 760.
- 26 Z. R. R. Tian, J. A. Voigt, J. Liu, B. Mckenzie and M. J. Mcdermott, *J. Am. Chem. Soc.*, 2002, **124**, 12954.
- 27 L. Vayssieres, *Adv. Mater.*, 2003, **15**, 464.
- 28 M. Yin, Y. Gu, I. L. Kuskovsky, T. Andelman, Y. M. Zhu, G. F. Neumark and S. O'Brien, *J. Am. Chem. Soc.*, 2004, **126**, 6206.
- 29 C.-C. Lin and Y.-Y. Li, *Mater. Chem. Phys.*, 2009, **113**, 334.
- 30 C.-C. Lin, W.-H. Lin and Y.-Y. Li, *J. Phys. D: Appl. Phys.*, 2008, **41**, 225411.
- 31 S. Baruah and J. Dutta, *Sci. Technol. Adv. Mater.*, 2009, **10**, 013001.
- 32 D. Polsongkrama, P. Chamninok, S. Pukird, L. Chow, O. Lupan, G. Chai, H. Khallaf, S. Park and A. Schulte, *Phys. B*, 2008, **403**, 3713.
- 33 S. Hussain, T. Liu, M. Kashif, L. Lin, S. Wu, W. Guo, W. Zeng and U. Hashim, *Mater. Sci. Semicond. Process.*, 2014, **18**, 52.
- 34 S. Xu, C. Lao, B. Weintraub and Z. L. Wang, *J. Mater. Res.*, 2008, **23**, 884.
- 35 H. Sowa and H. Ahsbabs, *J. Appl. Crystallogr.*, 2006, **39**, 169.
- 36 T. M. Sabine, B. A. Hunter, W. R. Sabine and C. J. Ball, *J. Appl. Crystallogr.*, 1998, **31**, 47.
- 37 P. Ballirano, *J. Appl. Crystallogr.*, 2003, **36**, 1056.
- 38 A. Katerinopoulou, T. Balic-Zunic and L. F. Lundegaard, *J. Appl. Crystallogr.*, 2012, **45**, 22.
- 39 M. Di Marco, M. Port, P. Couvreur, C. Dubernet, P. Ballirano and C. Sadun, *J. Am. Chem. Soc.*, 2006, **128**, 10054.
- 40 M. Di Marco, P. Ballirano, M. Port, E. Piscopiello, P. Couvreur, C. Dubernet and C. Sadun, *J. Mater. Chem.*, 2009, **19**, 6354.
- 41 P. Ballirano, C. De Vito, V. Ferrini and S. Mignardi, *J. Hazard. Mater.*, 2010, **178**, 522.
- 42 I. D. Brown and R. D. Shannon, *Acta Crystallogr., Sect. A: Cryst. Phys., Diffr., Theor. Gen. Crystallogr.*, 1973, **29**, 266.
- 43 I. A. Kaurova, G. M. Kuzmicheva and V. B. Rybakov, *Crystallogr. Rep.*, 2013, **58**, 226.
- 44 P. Ballirano and C. Sadun, *Struct. Chem.*, 2009, **20**, 815.
- 45 J. F. Moulder, W. F. Stickle, P. E. Sobol and K. D. Bomben, *Handbook of X-ray Photoelectron Spectroscopy*, ed. J. Chastain, Perkin-Elmer Corp., Physical Electronic Division, Eden Prairie, 2nd edn, 1992.
- 46 D. Barreca, A. Gasparotto, C. Maccato, C. Maragno and E. Tondello, *Surf. Sci. Spectra*, 2007, **14**, 19.
- 47 S. Kaciulis, L. Pandolfi, E. Comini, G. Faglia, M. Ferroni, G. Sberveglieri, S. Kandasamy, M. Shafiei and W. Wlodarski, *Surf. Interface Anal.*, 2008, **40**, 575.
- 48 S. Kaciulis, G. Mattogno, A. Galdikas, A. Mironas and A. Setkus, *J. Vac. Sci. Technol., A*, 1996, **14**, 3164.
- 49 M. Breedon, C. Rix and K. Kalantar-zadeh, *Mater. Lett.*, 2009, **63**, 249.
- 50 M. H. Huang, S. Mao, H. Feick, H. Q. Yan, Y. Y. Wu, H. Kind, E. Weber, R. Russo and P. D. Yang, *Science*, 2001, **292**, 1897.
- 51 A. B. Djuricic, Y. H. Leung, K. H. Tam, L. Ding, W. K. Ge, H. Y. Chen and S. Gwo, *Appl. Phys. Lett.*, 2006, **88**, 103107.
- 52 L. Wu, Y. Wu, X. Pan and F. Kong, *Opt. Mater.*, 2006, **28**, 418.
- 53 Y. Y. Tay, T. T. Tan, M. H. Liang, F. Boey and S. Li, *Phys. Chem. Chem. Phys.*, 2010, **12**, 6008.
- 54 I. Shalish, H. Temkin and V. Narayanamurti, *Phys. Rev. B: Condens. Matter Mater. Phys.*, 2004, **69**, 245401.
- 55 S. Jiang, Z. Ren, S. Gong, S. Yin, Y. Yu, X. Li, G. Xu, G. Shen and G. Han, *Appl. Surf. Sci.*, 2014, **289**, 252.
- 56 L. H. Quang, S. J. Chua, K. P. Loh and E. Fitzgerald, *J. Cryst. Growth*, 2006, **287**, 157.
- 57 T.-J. Liu, Q. Wang and P. Jiang, *RSC Adv.*, 2013, **3**, 12662.